

A Stochastic MIMO Radio Channel Model With Experimental Validation

Jean Philippe Kermaol, Laurent Schumacher, *Member, IEEE*, Klaus Ingemann Pedersen, *Member, IEEE*, Preben Elgaard Mogensen, *Member, IEEE*, and Frank Frederiksen

Abstract—Theoretical and experimental studies of multiple-input/multiple-output (MIMO) radio channels are presented in this paper. A simple stochastic MIMO model channel has been developed. This model uses the correlation matrices at the mobile station (MS) and base station (BS) so that results of the numerous single-input/multiple-output studies that have been published in the literature can be used as input parameters. In this paper, the model is simplified to the narrowband channels. The validation of the model is based upon data collected in both picocell and microcell environments. The stochastic model has also been used to investigate the capacity of MIMO radio channels, considering two different power allocation strategies, water filling and uniform and two different antenna topologies, 4×4 and 2×4 . Space diversity used at both ends of the MIMO radio link is shown to be an efficient technique in picocell environments, achieving capacities within 14 b/s/Hz and 16 b/s/Hz in 80% of the cases for a 4×4 antenna configuration implementing water filling at a SNR of 20 dB.

Index Terms—Eigenanalysis, multiple-input/multiple-output measurement, spectral efficiency, stochastic multiple-input/multiple-output radio channel model.

I. INTRODUCTION

THE REMARKABLE Shannon capacity available from deploying multiple antennas at both the transmitter (Tx) and the receiver (Rx) of a wireless system, has generated considerable interest in recent years [1], [2]. Large capacity is obtained via the potential decorrelation between the channel coefficient of the multiple-input/multiple-output (MIMO) radio channel, which can be exploited to create several parallel subchannels. However, the potential capacity gain is highly dependent on the multipath richness, since a fully correlated MIMO radio channel only offers one subchannel, while a completely decorrelated radio channel potentially offers multiple subchannels depending on the antenna configuration.

Following Telatar's seminal paper [3], most MIMO theoretical and simulation studies have assumed either fully correlated or fully decorrelated radio channels [1], [4], while a partially

correlated radio channel should be expected in practice. The objective of this study is, therefore, to derive and to empirically validate a simple MIMO radio channel model, which is applicable for link level simulations. Some authors, as in [5], have approached the problem from a geometrically-based perspective. In [5, p. 19], spatial fading correlation is introduced by extending the one-ring model of scatterers first used by Clarke [6, p. 60] to MIMO setups. A mathematical framework for a simple stochastic wideband MIMO radio channel model was presented in [7]. In this paper, we simplify the model by reformulating it for narrowband (NB) channels.

One of the main strengths of the proposed MIMO stochastic model is that it relies on a small set of parameters to fully characterize the communication scenario, namely the power gain of the MIMO channel matrix, two correlation matrices describing the correlation properties at both ends of the transmission links, and the associated Doppler spectrum of the channel paths. These parameters can be extracted from measurement results, but they can also be derived from single-input/multiple-output (SIMO) results already published in the open literature. Indeed, during the last decade, many studies have focused on SIMO radio channel models for the evaluation of adaptive antennas at the base station (BS) [8]–[12]. These models have mainly been derived from geometric scattering distributions [9], [10] or extensive analysis of measurement data [11], [12].

The validation of the model is supported by measurement results. Using two measurement setups exhibiting several transmit and receive elements, 107 paths, i.e., the radio link between the array at the mobile station (MS) and BS, have been investigated in seven different picocell and microcell environments. Parameters of the MIMO model are extracted from the measurement data and fed to the model such as to compare simulation results with the measurement results.

The paper is organized as follows. Section II introduces the stochastic MIMO radio channel model. In Section III, extensive MIMO measurement campaigns are presented, followed by the experimental validation of the stochastic model in Section IV. Finally, Section V presents capacity results in a single-user scenario based on simulated data generated by the proposed MIMO radio channel.

II. STOCHASTIC MIMO CHANNEL MODEL

A. General Description

Consider the MIMO setup pictured in Fig. 1 with M antennas at the BS and N antennas at the MS. The signals at the BS antenna array are denoted by the vector

Manuscript received March 15, 2001; revised February 22, 2002. This work was supported in part by the European Union IST Research Project METRA (Multi Element Transmit and Receive Antennas).

J. P. Kermaol and L. Schumacher are with the Center for PersonKommunikation, Niels Jernes Vej 12, DK-9220 Aalborg East, Denmark (e-mail: jpk@cpk.auc.dk; schum@cpk.auc.dk).

K. I. Pedersen and F. Frederiksen are with Nokia Networks, Niels Jernes Vej 10, DK-9220 Aalborg East, Denmark (e-mail: klaus.i.pedersen@nokia.com; frank.frederiksen@nokia.com).

P. E. Mogensen is with the Center for PersonKommunikation, Niels Jernes Vej 12 DK-9220 Aalborg East, Denmark and also with the Nokia Networks, Niels Jernes Vej 10, DK-9220 Aalborg East, Denmark (e-mail: pm@cpk.auc.dk).

Publisher Item Identifier 10.1109/JSAC.2002.801223.

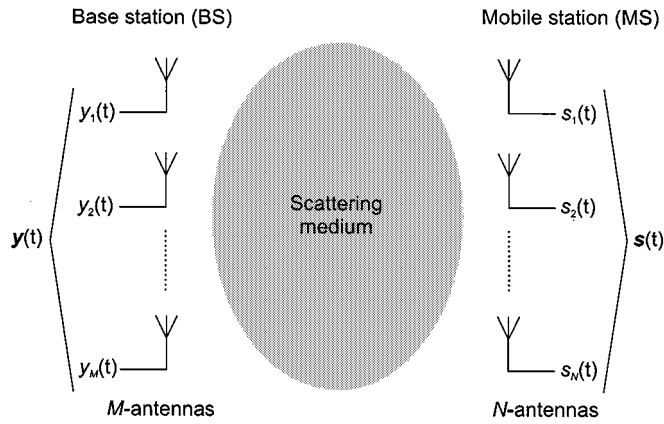


Fig. 1. Two antenna arrays in a scattering environment.

$\mathbf{y}(t) = [y_1(t), y_2(t), \dots, y_M(t)]^T$, where $y_m(t)$ is the signal at the m th antenna port and $[\cdot]^T$ denotes transposition. Similarly, the signals at the MS are $\mathbf{s}(t) = [s_1(t), s_2(t), \dots, s_N(t)]^T$.

A functional sketch of the MIMO radio channel is given in Fig. 3. The NB MIMO radio channel $\mathbf{H} \in \mathbb{C}^{M \times N}$ which describes the connection between the MS and the BS can be expressed as

$$\mathbf{H} = \begin{bmatrix} \alpha_{11} & \alpha_{12} & \cdots & \alpha_{1N} \\ \alpha_{21} & \alpha_{22} & \cdots & \alpha_{2N} \\ \vdots & \vdots & \ddots & \vdots \\ \alpha_{M1} & \alpha_{M2} & \cdots & \alpha_{MN} \end{bmatrix} \quad (1)$$

where α_{mn} is the complex transmission coefficient from antenna n at the MS to antenna m at the BS. For simplicity, it is assumed that α_{mn} is complex Gaussian distributed with identical average power. However, this latest assumption can be easily relaxed as shown in the Appendix. Thus, the relation between the vectors $\mathbf{y}(t)$ and $\mathbf{s}(t)$ can be expressed as

$$\mathbf{y}(t) = \mathbf{H}(t)\mathbf{s}(t). \quad (2)$$

B. Assumptions

It is assumed that all antenna elements in the two arrays have the same polarization and the same radiation pattern. The spatial complex correlation coefficient at the BS between antenna m_1 and m_2 is given by

$$\rho_{m_1 m_2}^{BS} = \langle \alpha_{m_1 n}, \alpha_{m_2 n} \rangle \quad (3)$$

where $\langle a, b \rangle$ computes the correlation coefficient between a and b . From (3), it is assumed that the spatial correlation coefficient at the BS is independent of n , since the n elements at the MS, illuminate the same surrounding scatterers and, therefore, also generate the same power azimuth spectrum (PAS) at the BS. Recall that the spatial correlation function is the Fourier transform of the PAS as discussed in [13]. Expressions of the spatial correlation function have been derived in the literature assuming that the PAS follows a cosine raised to an even integer [14], a Gaussian function [15], a uniform function [16], and a Laplacian function [17].

The spatial complex correlation coefficient observed at the MS is similarly defined as

$$\rho_{n_1 n_2}^{MS} = \langle \alpha_{m n_1}, \alpha_{m n_2} \rangle \quad (4)$$

and assumed to be independent of m . An approximate expression of the spatial correlation function averaged over all possible azimuth orientations of the MS array is derived in [19]. It appears as a function of the azimuth dispersion Λ with $\Lambda \in [0; 1]$, where $\Lambda = 0$ corresponds to a scenario where the power is coming from one distinct direction only, while $\Lambda = 1$ when the PAS is uniformly distributed over the azimuthal range $[0^\circ; 360^\circ]$ [18]. As the MS is typically nonstationary, the results presented in [19] are considered to be very useful since they are averaged over all orientations of the MS array.

Given (3) and (4), one can define the following symmetrical complex correlation matrices

$$\mathbf{R}_{BS} = \begin{bmatrix} \rho_{11}^{BS} & \rho_{12}^{BS} & \cdots & \rho_{1M}^{BS} \\ \rho_{21}^{BS} & \rho_{22}^{BS} & \cdots & \rho_{2M}^{BS} \\ \vdots & \vdots & \ddots & \vdots \\ \rho_{M1}^{BS} & \rho_{M2}^{BS} & \cdots & \rho_{MM}^{BS} \end{bmatrix}_{M \times M}$$

and

$$\mathbf{R}_{MS} = \begin{bmatrix} \rho_{11}^{MS} & \rho_{12}^{MS} & \cdots & \rho_{1N}^{MS} \\ \rho_{21}^{MS} & \rho_{22}^{MS} & \cdots & \rho_{2N}^{MS} \\ \vdots & \vdots & \ddots & \vdots \\ \rho_{N1}^{MS} & \rho_{N2}^{MS} & \cdots & \rho_{NN}^{MS} \end{bmatrix}_{N \times N} \quad (5)$$

for later use.

Finally, the correlation coefficient between two arbitrary transmission coefficients connecting two different sets of antennas is expressed as

$$\rho_{n_2 m_2}^{n_1 m_1} = \langle \alpha_{m_1 n_1}, \alpha_{m_2 n_2} \rangle \quad (6)$$

which is shown in the Appendix to be equivalent to

$$\rho_{n_2 m_2}^{n_1 m_1} = \rho_{n_1 n_2}^{MS} \rho_{m_1 m_2}^{BS} \quad (7)$$

provided that (3) and (4) are independent of n and m , respectively. In other words, this means that the spatial correlation matrix of the MIMO radio channel is the Kronecker product of the spatial correlation matrix at the MS and the BS and is given by

$$\mathbf{R}_{MIMO} = \mathbf{R}_{MS} \otimes \mathbf{R}_{BS} \quad (8)$$

where \otimes represents the Kronecker product. This has also been confirmed in [20].

C. Generation of Simulated Correlated Channel Coefficients

Correlated channel coefficients α_{mn} are generated from zero-mean complex independent identically distributed (i.i.d.) random variables a_{mn} shaped by the desired Doppler spectrum such that

$$\mathbf{A} = \mathbf{C}\mathbf{a} \quad (9)$$

where $\mathbf{A}_{MN \times 1} = [\alpha_{11}, \alpha_{21}, \dots, \alpha_{M1}, \alpha_{12}, \dots, \alpha_{MN}]^T$ and $\mathbf{a}_{MN \times 1} = [a_1, a_2, \dots, a_{MN}]^T$ where the symmetrical mapping matrix \mathbf{C} results from the standard Cholesky factorization of the matrix $\mathbf{R}_{MIMO} = \mathbf{C}\mathbf{C}^T$ provided that \mathbf{R}_{MIMO} is nonsingular [28]. Subsequently, the generation of the simulated MIMO channel matrix \mathbf{H} can be deduced from the vector \mathbf{A} . Note that the correlation matrices and the Doppler spectrum cannot be chosen independently, as they are connected through the PAS at the MS [21].

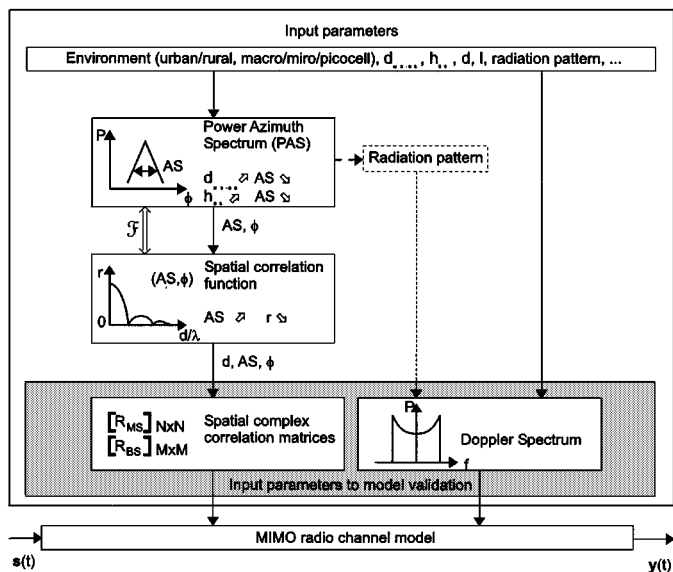


Fig. 2. Illustration of the two measurement setups.

D. Restriction to the Model

The pin hole [4] or keyhole [22] effect has been raised in previous work. This effect would occur when scattering regions surrounding both transmit and receive ends are separated by a screen with a small hole in the middle. In this case, the received signal between the antenna elements at both ends of the MIMO radio link are uncorrelated, but still \mathbf{H} would have low rank. Although data were collected in variety of environments, the pin hole or keyhole effect was not observed. Neither can the model reproduce this effect. This is explained by the fact that in [22] the transfer channel matrix is described as a dyad with one degree of freedom, where each channel coefficient writes as the product of two independent zero-mean complex Gaussian random variables. It is, therefore, not possible to claim that a linear generation process as described in (9) can account for the product of random variables.

III. MEASUREMENT CAMPAIGNS

The objectives of the measurement campaigns described in this section are to collect the data required to 1) validate the MIMO radio channel model and 2) estimate the model parameters that characterize different environments.

A. Measurement Setups

Two measurement setups are considered. They differ in the motion of the Tx and the antenna array topology of the Tx, as illustrated in Fig. 2 and described in [23] and [24]. In both setups, the Tx is at the MS and the stationary Rx is located at the BS. These two setups provide measurement results with different correlation properties of the MIMO channel for small antenna spacings of the order of 0.5λ or 1.5λ . The BS consists of four parallel Rx channels. The sounding signal is a MSK-modulated linear shift register sequence of a length of 127 chips, clocked at a chip rate of 4.096 Mcps. At the Rx, the channel sounding is performed within a window of $14.6 \mu s$, with a sampling resolution of 122 ns ($1/2$ chip period) to obtain an estimate of the

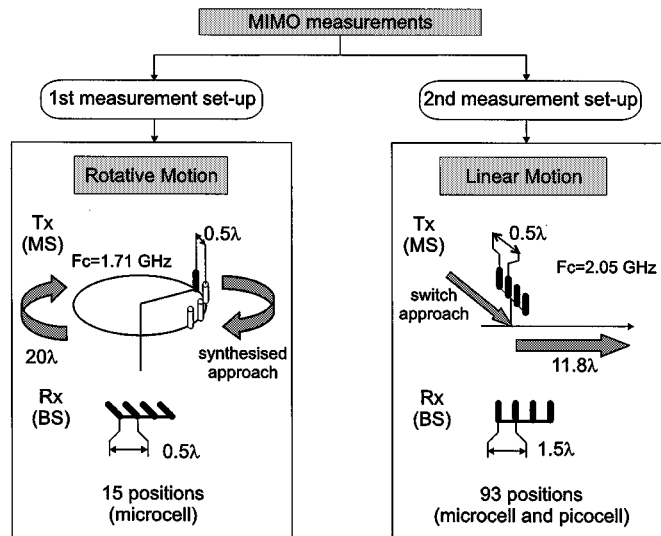


Fig. 3. Functional sketch of the MIMO model. d_{MS-BS} stands for distance between MS and BS, h_{BS} for the height of BS above ground floor, and AS for azimuth spread.

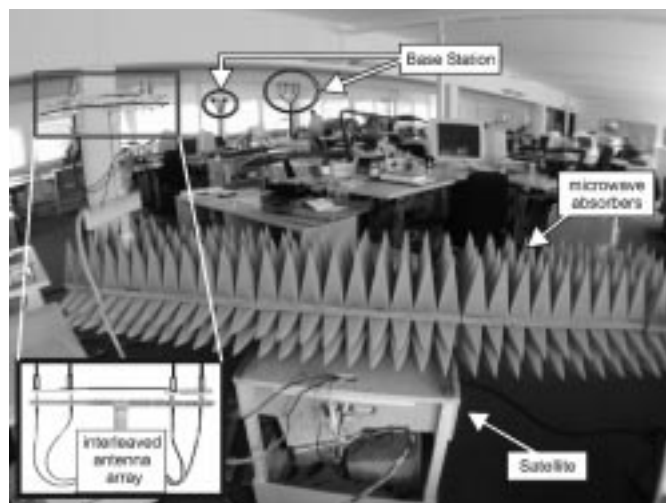


Fig. 4. Second measurement setup. The MS appears on the foreground with the "satellite" and its shield while the BS stands in the background.

complex impulse response (IR). The NB information is subsequently extracted by averaging the complex delayed signal components. A more thorough description of the stand-alone tested (i.e., Rx and Tx) is documented in [25].

1) *First Measurement Setup*: A standard vertically polarized dipole antenna (Fig. 3) is mounted on a rotating bar and describes a circumferential distance of 20λ where λ is the wavelength. The operating frequency is 1.71 GHz. A synthesized antenna array with a separation of 0.5λ between the antenna elements is considered in the post-processing analysis. A uniform linear antenna array with four elements polarized at $+45^\circ$ spaced by 0.45λ is used at the BS.

2) *Second Measurement Setup*: An interleaved antenna array with four vertically polarized sleeve dipoles elements mounted at the MS is moved along a linear slide over a distance of 11.8λ as shown in Fig. 4. Such an antenna arrangement is described in detail in [24] and is used to reduce the mutual

TABLE I
SUMMARY AND DESCRIPTION OF THE DIFFERENT MEASURED ENVIRONMENTS

Cell type	Environment	MS locations	Measurement setup	Description
microcell	A	15	1st	The indoor environment consists of small offices with windows metallicly shielded - 300 m between MS and BS
	B	13	2nd	The indoor environment consists of small offices - 31 to 36 m between MS and BS
picocell	C	21	2nd	The indoor environment is the same as in A
	D	12	2nd	Reception hall - Large open area
	E	18	2nd	Modern open office with windows metallicly shielded
	F	16	2nd	The indoor environment is the same as in B
	G	12	2nd	Airport - Very large indoor open area

coupling between the elements, thus, preserving the omnidirectionality of the radiation pattern of the antenna elements. After post processing, a linear array is derived from it with a spacing of 0.4λ . The Tx uses a 1-to-4 switch with a switch interval of $50 \mu\text{s}$ between each element of the antenna array, implementing a pseudo parallel transmission within $200 \mu\text{s}$. Note, the operating frequency is 2.05 GHz (UMTS band) for this setup. At the BS, a uniform linear array with four vertically polarized sleeve dipoles elements with a spacing of 1.5λ is employed. The MS consists of two trolleys where one trolley contains all the electronic hardware of the Tx and the other, later referred to as the "satellite," is equipped with the linear slide carrying the Tx antenna array. The two trolleys are connected by 10-m coaxial and signal cables. The purpose of using two trolleys is to reduce the effect of reflections from metallic surfaces. The satellite trolley is made of wood and the metallic part of the linear slide is shielded by microwave absorbers as shown in Fig. 4.

B. Environment

Channel data were collected in two types of environments: picocell and microcell. Here the term picocell and microcell refer to indoor-to-indoor and indoor-to-outdoor environment, respectively. The measurement campaigns are undertaken in several buildings at two main locations: the campus of Aalborg University and the Aalborg International Airport. Table I summarizes the environments.

For each environment (A–G), several MS locations are selected to provide a set of measurements where both line-of-sight (LOS) and non-LOS (NLOS) scenarios are present. Moreover, several BS locations are selected within the same environment in addition to the MS locations, as illustrated in Fig. 5, in order to increase the reachness of the data set. A total of 107 paths are investigated within these seven environments.

The first measurement setup is used to investigate 15 paths in a microcell environment, i.e., environment A in Table I. The MS is positioned in different locations inside a building while the BS is mounted on a crane and elevated above roof top level (i.e., 9 m) to provide direct LOS to the building. The antenna is

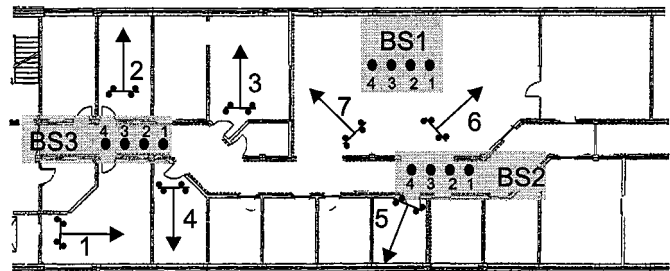


Fig. 5. Example of picocell environment C. The arrows represent the displacement of the MS (1 to 7). The three shaded areas represent the different positions of the BS, with the circles illustrating each antenna element of the array. In total, 21 paths are investigated for this environment.

located 300 m away from the building. The second setup is used to investigate 92 paths for both microcell and picocell environments, i.e., environment B and C to G, respectively, as shown in Table I. The distance between the BS and the MS is 31 to 36 m for microcell B, with the BS located outside.

The stochastic model relies on the wide sense stationary (WSS) condition, meaning that as a rule of thumb the scatterers should be 10 times the distance travelled by the MS away from it, which is equivalent to about 20 m in the present case. This condition can be questionable when considering practical measurements. Indeed, when measurements were undertaken in small rooms, the travelled distance of the MS was very similar to the distance of the MS to the wall, hence possibly not fulfilling the WSS condition. These restrictions need to be considered when discussing the validity of the simulated results.

IV. MODEL VALIDATION

The purpose of this section is four-fold: 1) to validate that the assumptions stated in the presented model apply to the measured data; 2) to introduce the input parameters used to validate the model; 3) to present the eigenanalysis used as benchmark in this validation process and, finally, 4) to illustrate the validation procedure and its outcome.

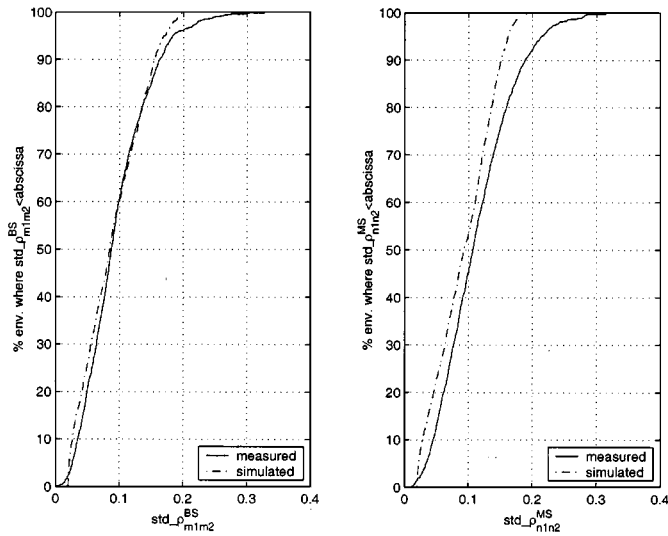


Fig. 6. Example of the cdf of $\text{std-}\rho_{m_1m_2}^{BS}$ (left graph) and $\text{std-}\rho_{n_1n_2}^{MS}$ (right graph). The cdf is performed over all the measured environments and for all the seven correlation coefficients.

A. Validation of the Stochastic MIMO Channel Model Assumptions

The validity of the underlying assumptions has been verified for a 4×4 MIMO configuration. These assumptions are that 1) the spatial correlation at the BS (3) and the MS (4) is independent of n and m , respectively, and 2) the spatial correlation matrix of the MIMO radio channel is the Kronecker product of the spatial correlation matrices at the BS and the MS (8).

Assumption 1): The standard deviation (std) of each measured spatial correlation coefficient $|\rho_{m_1m_2}^{BS}|$ and $|\rho_{n_1n_2}^{MS}|$ is computed over the N and M reference antennas, respectively, for each environment. The std at the BS is expressed as

$$\text{std-}\rho_{m_1m_2}^{BS} = \text{std}(\{|\rho_{m_1m_2}^{BS}\| \}), \quad \forall n \in [1 \dots 4] \quad (10)$$

and at the MS such that

$$\text{std-}\rho_{n_1n_2}^{MS} = \text{std}(\{|\rho_{n_1n_2}^{MS}\| \}), \quad \forall m \in [1 \dots 4]. \quad (11)$$

Fig. 6 presents the empirical cumulative distribution function (cdf) of $\text{std-}\rho_{m_1m_2}^{BS}$ (left graph) and $\text{std-}\rho_{n_1n_2}^{MS}$ (right graph) computed over the 92 paths considered with the second measurement setup for the six different correlation coefficients, i.e., the upper triangular coefficient of the correlation matrix, when a 4×4 MIMO configuration is used. To validate the statistical significance of the empirical results, the empirical cdf is compared with a cdf obtained from simulations performed under similar conditions. The matching of the two cdfs demonstrates that Assumption 1) is fulfilled, as explained here after.

For each of the 92×6 different measured correlation coefficients, two correlated, Rayleigh-distributed signals of length 1000λ are generated. These 1000λ -long vectors are truncated into 11.8λ -long runs over which the correlation coefficient is computed once again. Hence, a wider new set of correlation values is collected, exhibiting a standard deviation $\text{std}_{11.8\lambda}$. This operation is repeated 92×6 times. A simulated cdf of $\text{std}_{11.8\lambda}$ is then obtained under similar conditions than the measured cdf.

However, these two cdfs could differ in two ways. Since the simulated cdf has been computed from a larger set of statistics than the measured cdf, it could exhibit a steeper slope. On the other hand, should Assumption 1) not be fulfilled, the median point of the cdfs would not coincide.

The simulated cdf is shown in Fig. 6. The slope difference of these cdfs indicates the impact of the lack of measured statistics with respect to the simulations described here above. But the fairly good match between the measured and the simulated cdfs supports assumption (3) and (4).

Assumption 2): This assumption is validated by comparing results generated from the proposed MIMO radio channel model with measured data. This is presented in Section IV-D.

B. Input Parameters to the Validation of the MIMO Model

The input parameters used in the validation stage are illustrated by the shaded area of Fig. 3. They are 1) the average spatial complex correlation matrices \mathbf{R}_{BS} and \mathbf{R}_{MS} and 2) the associated average Doppler spectrum.

The measured spatial complex correlation matrices are the results of an average over the reference antennas n and m with respect to which the matrices are computed.

The averaged measured Doppler spectrum is obtained by averaging over all the MN channel coefficients. It is defined at the MS, since the BS is fixed. This limitation is due to the measurement setup implementation, but is not inherent to the model. If both MS and BS were moving, the Doppler spectrum of the channels would have been defined as the convolution of separate Doppler spectra defined either at the MS or at the BS, considering, respectively, the BS and the MS as fixed.¹ The corresponding complex coefficients of the vector \mathbf{a} (9) have their amplitudes shaped by the average measured Doppler spectrum and assigned a random phase uniformly distributed over $[0, 2\pi]$ such that MN independent and identically distributed variables are generated.

Two examples of typical paths have been selected from the set of paths described in Section III. Their differences in terms of propagation properties motivated this choice. Example 1 is one of the paths in the picocell environment C where the propagation scenario offers a decorrelated case. On the other hand, example 2 presents the opposite situation where the propagation scenario is correlated. This appears in one of the paths in the microcell environment A.

Example 1: Picocell Decorrelated.

See (12) at the bottom of the next page.

Example 2: Microcell Correlated.

See (13) at the bottom of the next page.

Both in Example 1 and 2, $|\mathbf{R}_{MS}|$ is decorrelated. This is expected since the MS is surrounded by scatterers. On the other hand, $|\mathbf{R}_{BS}|$ presents two different behaviors. In Example 1, the spatial correlation coefficients remain low as expected in the case of an indoor termination. On the other hand, the spatial correlation coefficients at the BS are highly correlated in Example 2 with a mean absolute value of the coefficient of 0.96. The high correlation is explained by the fact that regarding this specific

¹The phase shifts due to both movements add, causing the respective phasers to multiply each other, which is equivalent to the convolution of their Doppler spectra.

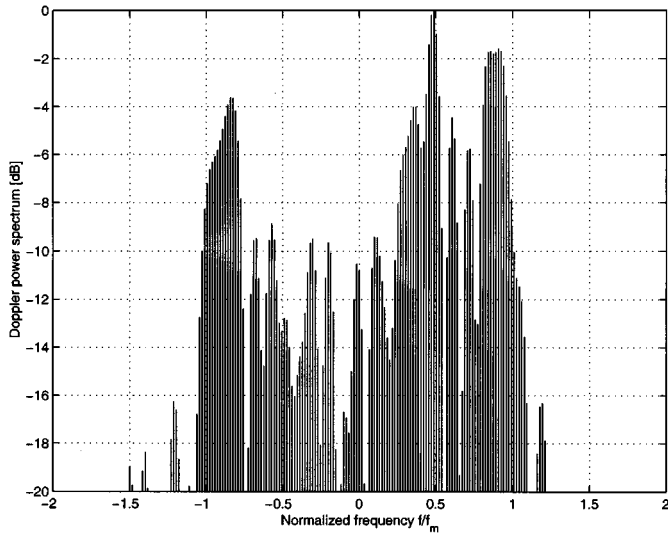


Fig. 7. Averaged measured Doppler power spectrum for Example 1 (picocell decorrelated).

example the BS is identified to be located above any surrounding scatterer. Therefore, it experienced a low azimuth spread (AS) which causes its antenna array elements to be highly correlated. An illustration of the averaged measured Doppler spectrum of Example 1 is presented in Fig. 7. The spectrum is normalized in frequency to its maximum Doppler shift f_m and in power to its maximum value.

C. The Eigenanalysis Method

The eigenvalue decomposition (EVD) of the instantaneous correlation matrix $\mathbf{R} = \mathbf{H}\mathbf{H}^H$ (not to be confused with \mathbf{R}_{MIMO}), where $[\cdot]^H$ represents Hermitian transposition, has been chosen to serve as a benchmark of the validation process. The channel matrix \mathbf{H} may offer K parallel subchannels with

different mean gains, with $K = \text{Rank}(\mathbf{R}) \leq \min(M, N)$ where the function $\text{Rank}(\cdot)$ and $\min(\cdot)$ return the rank of the matrix and the minimum value of the arguments, respectively, [26]. The k th eigenvalue can be interpreted as the power gain of the k th subchannel [26]. In the following, λ_k represents the eigenvalues. In order to assess the qualitative accuracy of the model, the comparison between measured and simulated eigenvalues is made for an antenna configuration where the largest number of eigenvalues is achievable within the limitation of the measurement setup antenna topology. This is the case for a 4×4 scenario since at most four eigenvalues can be expected. In the following, the eigenvalues are normalized to the mean power of the single Tx and a single Rx channel coefficient $1/(MN) \sum_{m=1}^M \sum_{n=1}^N |\alpha_{mn}|^2$.

D. Validation Procedure

For each of the 107 paths, the input parameters, presented in Section IV-B, are fed into the proposed stochastic MIMO model and a Monte Carlo simulation consisting of 100 iterations are performed to generate the elements of the simulated matrix $\tilde{\mathbf{H}}$. $\tilde{\mathbf{H}}$ is a three-dimensional (3-D) matrix ($M \times N \times L$), where L is the number of sample equivalent to the time domain definition in (2). For each iteration, the seed of the random generator which defines the phase of the complex coefficient of the vector \mathbf{a} is different.

At iteration q , $\tilde{\mathbf{H}}_{4 \times 4 \times L}$ counts as many samples L as in the measured $\mathbf{H}_{4 \times 4 \times L}$ collected during one antenna array run that is to say 20λ or 11.8λ depending of the measurement setup used. The EVD of $\tilde{\mathbf{H}}_{4 \times 4 \times l} \tilde{\mathbf{H}}_{4 \times 4 \times l}^H$ is then performed for each sample l in order to identify the corresponding simulated eigenvalues denoted by the vector $\lambda_{\text{sim_kq}_{L \times 1}} = [\lambda_{\text{sim_kq } 1}, \dots, \lambda_{\text{sim_kq } l}]^T$, $k = 1 \dots K$.

From these eigenvalues, k vectors $[\lambda_{\text{sim_k}}]_{1 \times QL}$ containing the 100 iterations of the simulated eigenvalues $\lambda_{\text{sim_kq}}$ are deduced so that $\lambda_{\text{sim_k}} = \{\lambda_{\text{sim_kq}}\}$ where $\{\cdot\}$ represents a set of

$$\mathbf{R}_{\text{BS}} = \begin{bmatrix} 1 & -0.45 + 0.53i & 0.37 - 0.22i & 0.19 + 0.21i \\ -0.45 - 0.53i & 1 & -0.35 - 0.02i & 0.02 - 0.27i \\ 0.37 + 0.22i & -0.35 + 0.02i & 1 & -0.10 + 0.54i \\ 0.19 - 0.21i & 0.02 + 0.27i & -0.10 - 0.54i & 1 \end{bmatrix}$$

$$\mathbf{R}_{\text{MS}} = \begin{bmatrix} 1 & -0.13 - 0.62i & -0.49 + 0.23i & 0.15 + 0.28i \\ -0.13 + 0.62i & 1 & -0.13 - 0.52i & -0.38 + 0.12i \\ -0.49 - 0.23i & -0.13 + 0.52i & 1 & 0.02 - 0.61i \\ 0.15 - 0.28i & -0.38 - 0.12i & 0.02 + 0.61i & 1 \end{bmatrix} \quad (12)$$

$$\mathbf{R}_{\text{BS}} = \begin{bmatrix} 1 & -0.61 + 0.77i & 0.14 - 0.94i & 0.24 + 0.89i \\ -0.61 - 0.77i & 1 & -0.85 + 0.50i & 0.57 - 0.78i \\ 0.14 + 0.94i & -0.85 - 0.50i & 1 & -0.91 + 0.40i \\ 0.24 - 0.89i & 0.57 + 0.78i & -0.91 - 0.40i & 1 \end{bmatrix}$$

$$\mathbf{R}_{\text{MS}} = \begin{bmatrix} 1 & -0.12 - 0.18i & 0.08 + 0.05i & -0.02 - 0.13i \\ -0.12 + 0.18i & 1 & -0.17 - 0.16i & 0.11 + 0.04i \\ 0.08 - 0.05i & -0.17 + 0.16i & 1 & -0.17 - 0.16i \\ -0.02 + 0.13i & 0.11 - 0.04i & -0.17 + 0.16i & 1 \end{bmatrix} \quad (13)$$

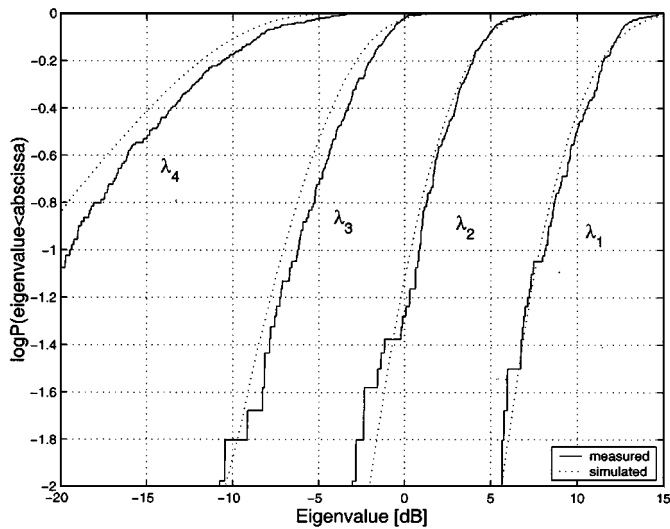


Fig. 8. Local validation. Cdf of λ_{meas_k} and λ_{sim_k} from Example 1 (picocell decorrelated).

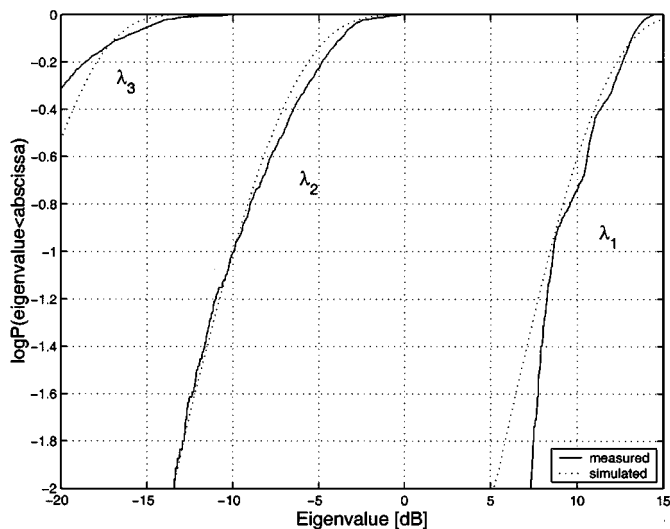


Fig. 9. Local validation. Cdf of λ_{meas_k} and λ_{sim_k} from Example 2 (microcell correlated).

variables. For the measured data, the eigenvalues were deduced so that $\lambda_{\text{meas}_k L \times 1} = [\lambda_{\text{meas}_k 1}, \dots, \lambda_{\text{meas}_k l}]^T$.

1) *Local Validation*: The local validation consists of the matching comparison between the cdf of λ_{meas_k} and λ_{sim_k} for each of the 107 paths. Figs. 8 and 9 present the eigenanalysis performed on the two propagation environments, Example 1 and 2, respectively. The cdfs of the measured eigenvalues λ_{meas_k} for a full run of the Tx antenna array are displayed with a solid line. On the same graph the cdfs of the simulated eigenvalues λ_{sim_k} are illustrated by a dashed line. Their cdfs have been performed over the QL variables of the vector λ_{sim_k} .

Inspection of Figs. 8 and 9 reveals that the cdfs of the eigenvalues generated by the stochastic model closely match those estimated using measured data.

2) *Global Validation*: A global analysis encompassing all the 107 paths has been performed in order to measure the difference between the measured and the simulated results. The com-

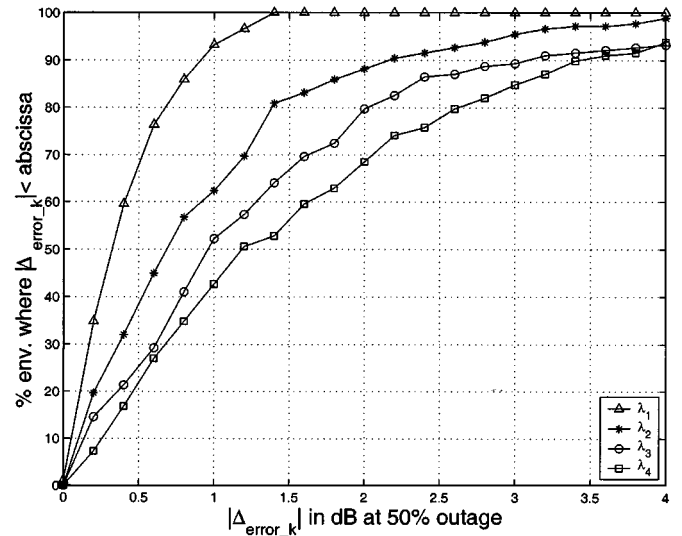


Fig. 10. Global validation. Cdf of $|\Delta_{\text{error}_k}|$ over the 107 paths.

parison is based on the difference between λ_{meas_k} and λ_{sim_k} at 50% ($\log_{10}(.5) = -0.3$) outage level for each paths and for each eigenvalue such that $\Delta_{\text{error}_k} = [\lambda_{\text{meas}_k} - \lambda_{\text{sim}_k}]_{50\%}$. For more clarity in the graph, the absolute value $|\Delta_{\text{error}_k}|$ is considered since Δ_{error_k} is symmetrical around zero. Despite the expected discrepancies between empirical and simulated results, one can see from Fig. 10 that the error generated by the proposed model is bounded by ± 0.6 dB for the strongest simulated eigenvalue λ_{sim_1} , by ± 1.6 dB for λ_{sim_2} , by ± 2.2 dB for λ_{sim_3} and by ± 2.7 dB for the weakest one, for 90% of the paths. These values are considered to be small error boundaries and it can be concluded that the proposed stochastic MIMO radio channel model has been validated.

V. SPECTRAL EFFICIENCY—SINGLE-USER SCENARIO

This section investigates the spectral efficiency of MIMO channels. This study is limited to single-user scenarios. Two power allocation strategies are compared in the following, simultaneously with two antenna array topologies.

A. Definition of the Power Allocation Schemes

In the situation where the channel is known at both Tx and Rx and is used to compute the optimum weight, the power gain in the k th subchannel is given by the k th eigenvalue, i.e., the signal-to-noise ratio (SNR) for the k th subchannel equals

$$\gamma_k = \lambda_k \frac{P_k}{\sigma_N^2} \quad (14)$$

where P_k is the power assigned to the k th subchannel, λ_k is the k th eigenvalue and σ_N^2 is the noise power. For simplicity, it is assumed that $\sigma_N^2 = 1$. According to Shannon, the maximum capacity² of K parallel subchannels equals [26]

$$C = \sum_{k=1}^K \log_2(1 + \gamma_k) \quad (15)$$

²The capacity expressions given throughout the paper are normalized with respect to the bandwidth, i.e., they are given in terms of b/s/Hz (spectral efficiency).

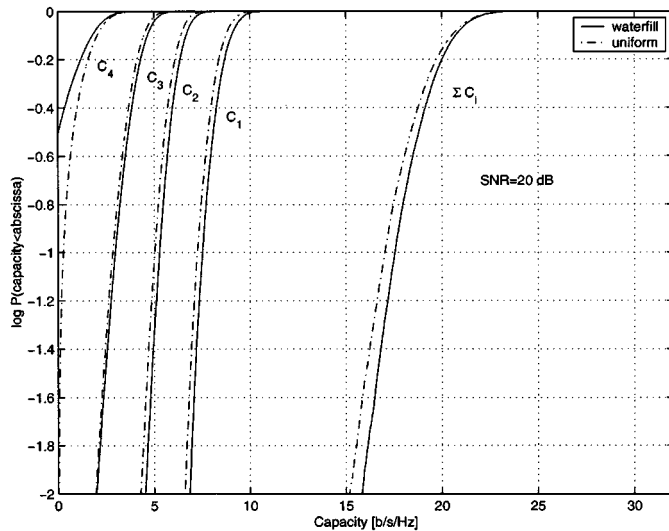


Fig. 11. Cdf of the capacity per subchannel C_k and its total results $\sum C_i$ for Example 1 (picocell decorrelated). A 4×4 antenna topology is presented here.

$$= \sum_{k=1}^K \log_2 \left(1 + \lambda_k \frac{P_k}{\sigma_N^2} \right) \quad (16)$$

where the mean SNR is defined as

$$\text{SNR} = \frac{\mathbf{E}[P_{Rx}]}{\sigma_N^2} = \frac{\mathbf{E}[P_{Tx}]}{\sigma_N^2}. \quad (17)$$

Given the set of eigenvalues $\{\lambda_k\}$, the power P_k allocated to each subchannel k is determined to maximize the capacity by using Gallager's water filling theorem [26] such that each subchannel is filled up to a common level D , i.e.,

$$\frac{1}{\lambda_1} + P_1 = \dots = \frac{1}{\lambda_K} + P_K = \dots = D \quad (18)$$

with a constraint on the total Tx power such that

$$\sum_{k=1}^K P_k = P_{Tx} \quad (19)$$

where P_{Tx} is the total transmitted power. This means that the subchannel with the highest gain is allocated with the largest amount of power. In the case where $1/\lambda_k > D$ then $P_k = 0$.

When the uniform power allocation scheme is employed, the power P_k is adjusted according to

$$P_1 = \dots = P_K. \quad (20)$$

Thus, in the situation where the channel is unknown, the uniform distribution of the power is applicable over the antennas [26] so that the power should be equally distributed between the N elements of the array at the Tx, i.e.,

$$P_n = \frac{P_{Tx}}{N}, \quad \forall n = 1 \dots N. \quad (21)$$

B. Impact of the Orthogonal Subchannels on Spectral Efficiency

Fig. 11 illustrates the impact of each subchannel upon the total capacity available for a 4×4 antenna configuration in the context of Example 1 at $\text{SNR} = 20$ dB. Here, C_k is the capacity of the k th subchannel of Fig. 8. When looking at the

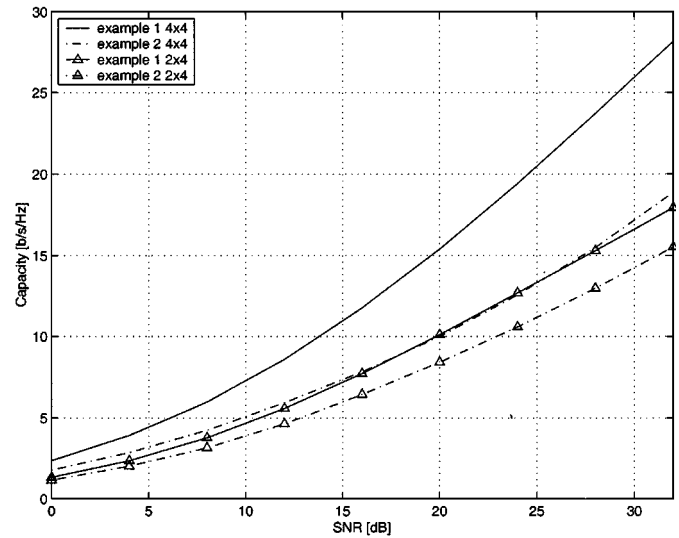


Fig. 12. Capacity (10% level) versus SNR for Example 1 (picocell decorrelated) and Example 2 (microcell-correlated).

10% outage of Fig. 11, one can conclude that the total capacity $\sum C_i$ is 17 b/s/Hz. This remarkable spectral efficiency is due to the contribution of the significant λ_1 , λ_2 , and λ_3 depicted in Fig. 8. From Fig. 11, one can also see that the difference between the two power allocation strategies is very small when the elements of the antenna array are sufficiently decorrelated [5, p. 64]. However, it must be emphasized that the water filling scheme provides a higher capacity than the uniform power distribution.

C. Antenna Setup and SNR Impacts

Fig. 12 illustrates the total capacity from Fig. 11 at the 10% level for different SNRs when the water filling power allocation scheme is used. Two antenna setups, a 4×4 and a 2×4 , are compared. On the same figure, the decorrelated and the correlated propagation scenarios are presented: Example 1 and 2. Three conclusions can be drawn from these examples.

- 1) One can see that the decorrelated situation provides more capacity than the correlated one at the same SNR and generally the total capacity increases with the SNR.
- 2) In the decorrelated scenario (Example 1), the 4×4 antenna configuration takes full advantage of its additional subchannel compared with the 2×4 .
- 3) The influence on the number of subchannels on the total capacity is illustrated for various SNRs. The capacity increases in a linear manner as a function of the SNR on a log scale while the slope increase proportionally with the number of subchannels in (15). At a low SNR, the contribution of the strongest subchannel is predominant. For a higher SNR, all the subchannels contribute to the total capacity. As a consequence, one can see that for a high SNR the slope of the 4×4 antenna array setup is twice the slope of the 2×4 one when comparing the two antenna array configurations, since only two parallel subchannels are achieved in the second antenna setup compared with the four parallel subchannels achievable by the 4×4 one. This is an important observation, since it implies that 1) at

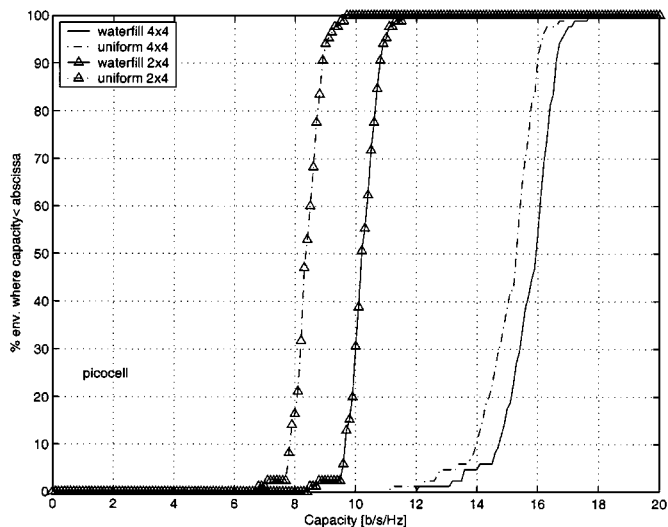


Fig. 13. Cdf over all the 79 (picocell) paths of the total capacity deduced from Fig. 12 at SNR = 20 dB for 4×4 and 2×4 antenna configuration.

low SNRs, the MIMO concept only provides a combined Tx and Rx diversity and 2) at high SNRs the MIMO system offers parallel channeling.

D. Spectral Efficiency Performance Per Cell Type

The capacity resulting from Fig. 12 and taken at a fixed SNR of 20 dB is extracted for all the 79 paths in picocell scenario and its cdf is presented in Fig. 13. It is seen that the offered capacity is fairly constant for the picocell environments, since the capacity results equal 14 b/s/Hz and 16 b/s/Hz at the 10% and 90% outage levels, respectively. This is explained by the fact that the elements of the antenna arrays at both the BS and the MS are sufficiently decorrelated in picocell (indoor to indoor) environments. In the context of a MIMO scenario this is interesting since multiple parallel subchannels are available. It can, therefore, be concluded that, even in situations where LOS is present, a MIMO topology using space diversity with small spacing is applicable for picocell environments.

Similarly to Fig. 13, Fig. 14 presents the cdf of the capacity derived from the 28 paths in the microcell scenario. One can see that contrary to the scenario in Fig. 13, the estimated capacity exhibits a much larger variation. This is explained by the use of two different antenna spacings to estimate the input parameters. The capacity varying from 12 b/s/Hz to 16 b/s/Hz is attributed to the setup using 1.5λ while the low capacity contribution from 9 to 12 b/s/Hz is obtained when applying only 0.5λ .

E. Consideration on the Spatial Domain in a MIMO Perspective

It is mentioned in [23] that when using 0.5λ separation at the BS, the correlation between the elements of the antenna array could vary from a correlated to a decorrelated situation which is explained by the fact that the BS experiences a low AS, especially when positioned above surrounding scatterers, which cause its antenna elements to be highly correlated (Section IV-B, Example 2). On the other hand, when the AS becomes larger, i.e., when the influence of the surrounding scatterers becomes more significant, the correlation between the antenna array elements decreases.

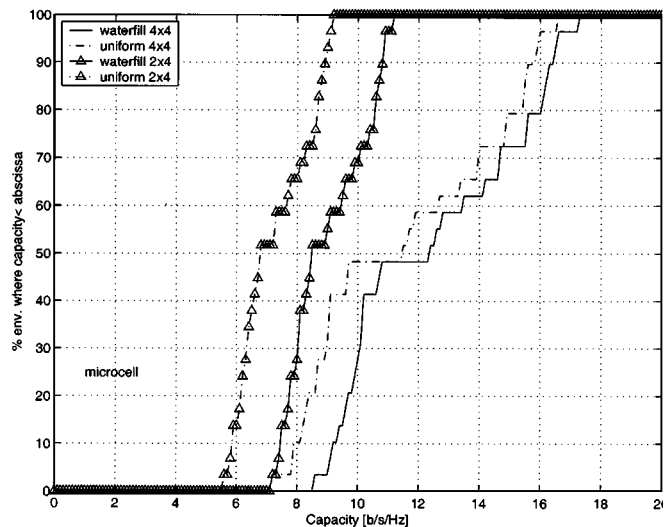


Fig. 14. Cdf over all the 28 (microcell) paths of the total capacity deduced from Fig. 12 at SNR = 20 dB for 4×4 and 2×4 antenna configuration.

This highlights the fact that in microcell environments, the correlation is strongly influenced by the change in the surrounding scatterers and also by the separation used in the antenna array. Therefore, the use of space diversity technique, on its own, is not recommended for a MIMO topology when using 0.5λ antenna spacing at the BS. However, when 1.5λ is employed, microcell capacity results indicate similar results as for the picocell environment.

VI. CONCLUDING REMARKS

In this paper, a stochastic MIMO radio channel model has been introduced and successfully validated in the NB condition by comparing measured and simulated results. It has been shown that the eigenvalues distribution of the model matches the measurements. The advantage of the proposed model is that its configuration, as far as time variation and spatial correlation are concerned, can rely on SIMO results previously published in the open literature. As such, it can be used for link-level simulation studies, as illustrated by the derivation of theoretical capacity limits. It is shown that space diversity used at both ends of the MIMO radio link is an efficient technique in picocell environments, achieving capacities between 14 b/s/Hz and 16 b/s/Hz in 80% of the cases for a 4×4 antenna configuration implementing water-filling at a SNR of 20 dB.

APPENDIX PROOF OF (7)

Consider the 2×2 correlated setup pictured in Fig. 15. The complex correlation coefficients μ and ρ are defined such as

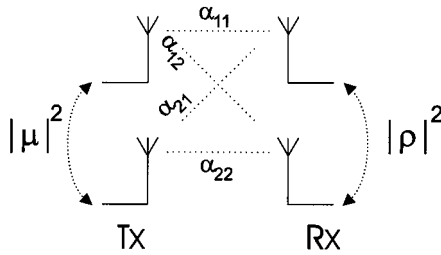
$$\mu = \langle \alpha_{11}, \alpha_{21} \rangle = \langle \alpha_{12}, \alpha_{22} \rangle \quad (22)$$

$$= \langle \alpha_{21}, \alpha_{11} \rangle^* = \langle \alpha_{22}, \alpha_{12} \rangle^* \quad (23)$$

$$\rho = \langle \alpha_{11}, \alpha_{12} \rangle = \langle \alpha_{21}, \alpha_{22} \rangle \quad (24)$$

$$= \langle \alpha_{12}, \alpha_{11} \rangle^* = \langle \alpha_{22}, \alpha_{21} \rangle^* \quad (25)$$

where α^* is the conjugate of α .

Fig. 15. 2×2 correlated setup.

On the other hand, the power correlation coefficient between antennas at the Tx is equal to $|\mu|^2$. Similarly, the power correlation coefficient between the two receiving antenna elements is set to $|\rho|^2$. In terms of channel transfer functions, this is given by

$$|\mu|^2 = \langle |\alpha_{11}|^2, |\alpha_{21}|^2 \rangle \quad (26)$$

$$= \langle |\alpha_{12}|^2, |\alpha_{22}|^2 \rangle \quad (27)$$

$$|\rho|^2 = \langle |\alpha_{11}|^2, |\alpha_{12}|^2 \rangle \quad (28)$$

$$= \langle |\alpha_{21}|^2, |\alpha_{22}|^2 \rangle. \quad (29)$$

Note that all these definitions assume that the correlation between two given antenna elements at one end does not depend on the antenna used as a reference at the other end. This assumption is fulfilled if all antenna elements of a given end exhibit the same radiation pattern.

Taking into account the fact that correlation matrices are Hermitian [27, p. 101], the complex correlation matrices are defined as follows:

$$\mathbf{R}_{Tx} = \begin{bmatrix} 1 & \mu \\ \mu^* & 1 \end{bmatrix} \quad (30)$$

$$\mathbf{R}_{Rx} = \begin{bmatrix} 1 & \rho \\ \rho^* & 1 \end{bmatrix}. \quad (31)$$

Note that \mathbf{R}_{Tx} and \mathbf{R}_{Rx} can be replaced by \mathbf{R}_{MS} and \mathbf{R}_{BS} in up-link or \mathbf{R}_{BS} and \mathbf{R}_{MS} in down-link, respectively. The purpose of this Appendix is to demonstrate that correlated channel transfer functions can be generated from the Kronecker product of the two complex correlation matrices. More particularly, it aims at demonstrating that the complex correlation between channel coefficients α_{11} and α_{22} or, identically, between α_{12} and α_{21} , is the product of the antenna complex correlation coefficients μ and ρ .

The Kronecker product of matrices (30) and (31) is given by

$$\mathbf{R}_{MIMO} = \mathbf{R}_{Tx} \otimes \mathbf{R}_{Rx} \quad (32)$$

$$= \begin{bmatrix} 1 & \rho & \mu & \mu\rho \\ \rho^* & 1 & \mu\rho^* & \mu \\ \mu^* & \mu^*\rho & 1 & \rho \\ \mu^*\rho^* & \mu^* & \rho^* & 1 \end{bmatrix}. \quad (33)$$

Let $\mathbf{a} = [w, x, y, z]^T$ be a vector of four complex zero-mean, unit variance independent random variables. As described in Section II, correlated channel coefficients α_{mn} are generated from the variable of the vector \mathbf{a} using the Cholesky decomposition of the matrix $\mathbf{\Gamma}$ as illustrated in Fig. 16. $\mathbf{\Gamma}$ results from the product of \mathbf{R}_{MIMO} by a power-shaping matrix \mathbf{P} when any imbalance in BPR (Branch Power Ratio) between antenna elements occurs. The elements of \mathbf{P} are the product of the standard deviations $\sigma_{\alpha_{mn}}$ of the channel coefficients α_{mn} . $\mathbf{\Gamma}$ is given by the following element-by-element product. See (34)–(36) at the bottom of the page.

Applying the Gaxpy algorithm [28, p. 143], the lower-triangular matrix \mathbf{C} , result of the Cholesky decomposition of $\mathbf{\Gamma}$, is given by (37) shown at the bottom of the page.

$$\mathbf{\Gamma} = \mathbf{R}_{MIMO} \times \mathbf{P} \quad (34)$$

$$= \begin{bmatrix} 1 & \rho & \mu & \mu\rho \\ \rho^* & 1 & \mu\rho^* & \mu \\ \mu^* & \mu^*\rho & 1 & \rho \\ \mu^*\rho^* & \mu^* & \rho^* & 1 \end{bmatrix} \times \begin{bmatrix} \sigma_{\alpha_{11}}^2 & \sigma_{\alpha_{11}}\sigma_{\alpha_{12}} & \sigma_{\alpha_{11}}\sigma_{\alpha_{21}} & \sigma_{\alpha_{11}}\sigma_{\alpha_{22}} \\ \sigma_{\alpha_{12}}\sigma_{\alpha_{11}} & \sigma_{\alpha_{12}}^2 & \sigma_{\alpha_{12}}\sigma_{\alpha_{21}} & \sigma_{\alpha_{12}}\sigma_{\alpha_{22}} \\ \sigma_{\alpha_{21}}\sigma_{\alpha_{11}} & \sigma_{\alpha_{21}}\sigma_{\alpha_{12}} & \sigma_{\alpha_{21}}^2 & \sigma_{\alpha_{21}}\sigma_{\alpha_{22}} \\ \sigma_{\alpha_{22}}\sigma_{\alpha_{11}} & \sigma_{\alpha_{22}}\sigma_{\alpha_{12}} & \sigma_{\alpha_{22}}\sigma_{\alpha_{21}} & \sigma_{\alpha_{22}}^2 \end{bmatrix} \quad (35)$$

$$= \begin{bmatrix} \sigma_{\alpha_{11}}^2 & \sigma_{\alpha_{11}}\sigma_{\alpha_{12}}\rho & \sigma_{\alpha_{11}}\sigma_{\alpha_{21}}\mu & \sigma_{\alpha_{11}}\sigma_{\alpha_{22}}\mu\rho \\ \sigma_{\alpha_{12}}\sigma_{\alpha_{11}}\rho^* & \sigma_{\alpha_{12}}^2 & \sigma_{\alpha_{12}}\sigma_{\alpha_{21}}\mu\rho^* & \sigma_{\alpha_{12}}\sigma_{\alpha_{22}}\mu \\ \sigma_{\alpha_{21}}\sigma_{\alpha_{11}}\mu^* & \sigma_{\alpha_{21}}\sigma_{\alpha_{12}}\mu^*\rho & \sigma_{\alpha_{21}}^2 & \sigma_{\alpha_{21}}\sigma_{\alpha_{22}}\rho \\ \sigma_{\alpha_{22}}\sigma_{\alpha_{11}}\mu^*\rho^* & \sigma_{\alpha_{22}}\sigma_{\alpha_{12}}\mu^* & \sigma_{\alpha_{22}}\sigma_{\alpha_{21}}\rho^* & \sigma_{\alpha_{22}}^2 \end{bmatrix}. \quad (36)$$

$$\mathbf{C} = \begin{bmatrix} \sigma_{\alpha_{11}} & 0 & 0 & 0 \\ \sigma_{\alpha_{12}}\rho^* & \sigma_{\alpha_{12}}\sqrt{1-|\rho|^2} & 0 & 0 \\ \sigma_{\alpha_{21}}\mu^* & 0 & \sigma_{\alpha_{21}}\sqrt{1-|\mu|^2} & 0 \\ \sigma_{\alpha_{22}}\mu^*\rho^* & \sigma_{\alpha_{22}}\mu^*\sqrt{1-|\rho|^2} & \sigma_{\alpha_{22}}\rho^*\sqrt{1-|\mu|^2} & \sigma_{\alpha_{22}}\sqrt{1+|\mu|^2|\rho|^2-|\mu|^2-|\rho|^2} \end{bmatrix}. \quad (37)$$

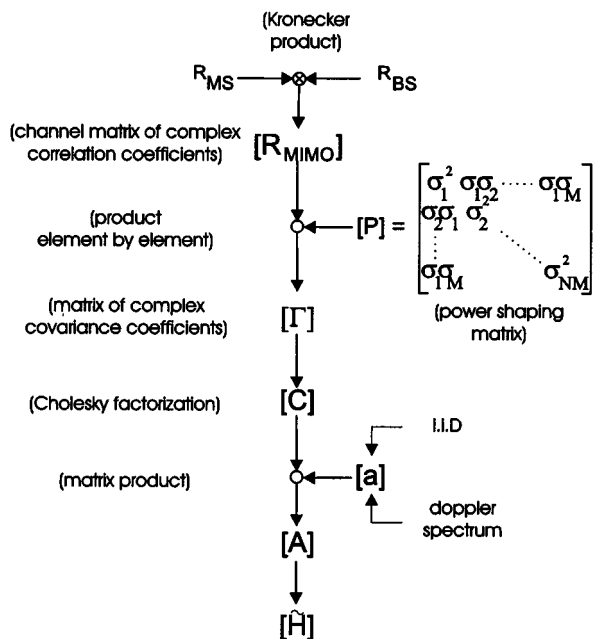


Fig. 16. Flow chart illustrating the practical procedure to obtain correlated channel coefficient.

Defining $\mathbf{A} = [\alpha_{11}, \alpha_{12}, \alpha_{21}, \alpha_{22}]^T$, the channel coefficients α_{ij} are generated as

$$\mathbf{A} = \mathbf{C}\mathbf{a} \quad (38)$$

$$\begin{bmatrix} \alpha_{11} \\ \alpha_{12} \\ \alpha_{21} \\ \alpha_{22} \end{bmatrix} = \mathbf{C} \begin{bmatrix} w \\ x \\ y \\ z \end{bmatrix}. \quad (39)$$

The next task is to demonstrate that these channel coefficients are correlated in the appropriate way.

The $4 \times 4 = 16$ complex correlation coefficients are derived as follows (\mathbf{E} stands for the mathematical expectation operator)

$$\langle \alpha_{11}, \alpha_{11} \rangle = \frac{\mathbf{E}[\alpha_{11}\alpha_{11}^*]}{\sigma_{\alpha_{11}}^2} \quad (40)$$

$$= \frac{\mathbf{E}[\sigma_{\alpha_{11}} w \sigma_{\alpha_{11}} w^*]}{\sigma_{\alpha_{11}}^2} \quad (41)$$

$$= \frac{\sigma_{\alpha_{11}}^2 \mathbf{E}[ww^*]}{\sigma_{\alpha_{11}}^2} \quad (42)$$

$$= 1 \quad (43)$$

since w has unit variance.

$$\langle \alpha_{11}, \alpha_{12} \rangle = \frac{\mathbf{E}[\alpha_{11}\alpha_{12}^*]}{\sigma_{\alpha_{11}}\sigma_{\alpha_{12}}} \quad (44)$$

$$= \frac{\mathbf{E}\left[\sigma_{\alpha_{11}} w \left(\sigma_{\alpha_{12}} \rho^* w + \sigma_{\alpha_{12}} \sqrt{1-|\rho|^2} x\right)^*\right]}{\sigma_{\alpha_{11}}\sigma_{\alpha_{12}}} \quad (45)$$

$$= \frac{\sigma_{\alpha_{11}}\sigma_{\alpha_{12}}\rho\mathbf{E}[ww^*] + \sigma_{\alpha_{11}}\sigma_{\alpha_{12}}\sqrt{1-|\rho|^2}\mathbf{E}[wx^*]}{\sigma_{\alpha_{11}}\sigma_{\alpha_{12}}} \quad (46)$$

$$= \rho \quad (47)$$

because the random variables in \mathbf{a} are independent, see (48)–(53) shown at the bottom of the page and (54)–(55) shown at the top of the next page. Outcomes (43), (47), (51), and (55) match the first line of \mathbf{R}_{MIMO} as shown in (56)–(73) on the next page. Relations (59), (64), (68), and (73) fill the second line of \mathbf{R}_{MIMO} , see (74)–(91). Outcomes (77), (81), (86), and (91) match the third line of \mathbf{R}_{MIMO} . Finally, see (92)–(110). Relations (95), (100), (105), and (110) achieve the filling of \mathbf{R}_{MIMO} and successfully conclude the demonstration. The validity of (7) is proved. This proof can easily be extended to the general $(M \times N)$ setup.

$$\langle \alpha_{11}, \alpha_{21} \rangle = \frac{\mathbf{E}[\alpha_{11}\alpha_{21}^*]}{\sigma_{\alpha_{11}}\sigma_{\alpha_{21}}} \quad (48)$$

$$= \frac{\mathbf{E}\left[\sigma_{\alpha_{11}} w \left(\sigma_{\alpha_{21}} \mu^* w + \sigma_{\alpha_{21}} \sqrt{1-|\mu|^2} y\right)^*\right]}{\sigma_{\alpha_{11}}\sigma_{\alpha_{21}}} \quad (49)$$

$$= \frac{\sigma_{\alpha_{11}}\sigma_{\alpha_{21}}\mu\mathbf{E}[ww^*] + \sigma_{\alpha_{11}}\sigma_{\alpha_{21}}\sqrt{1-|\mu|^2}\mathbf{E}[wy^*]}{\sigma_{\alpha_{11}}\sigma_{\alpha_{21}}} \quad (50)$$

$$= \mu \quad (51)$$

$$\langle \alpha_{11}, \alpha_{22} \rangle = \frac{\mathbf{E}[\alpha_{11}\alpha_{22}^*]}{\sigma_{\alpha_{11}}\sigma_{\alpha_{22}}} \quad (52)$$

$$= \frac{1}{\sigma_{\alpha_{11}}\sigma_{\alpha_{22}}} \mathbf{E}\left[\sigma_{\alpha_{11}} w \left(\sigma_{\alpha_{22}} \mu^* \rho^* w + \sigma_{\alpha_{22}} \mu^* \sqrt{1-|\rho|^2} x + \sigma_{\alpha_{22}} \rho^* \sqrt{1-|\mu|^2} y + \sigma_{\alpha_{22}} \sqrt{1+|\mu|^2} |\rho|^2 z - |\mu|^2 - |\rho|^2 z\right)^*\right] \quad (53)$$

$$= \frac{1}{\sigma_{\alpha_{11}}\sigma_{\alpha_{22}}} \left\{ \begin{aligned} &\sigma_{\alpha_{11}}\sigma_{\alpha_{22}}\mu\rho\mathbf{E}[ww^*] + \sigma_{\alpha_{11}}\sigma_{\alpha_{22}}\mu\sqrt{1-|\rho|^2}\mathbf{E}[wx^*] \\ &+ \sigma_{\alpha_{11}}\sigma_{\alpha_{22}}\rho\sqrt{1-|\mu|^2}\mathbf{E}[wy^*] \\ &+ \sigma_{\alpha_{11}}\sigma_{\alpha_{22}}\sqrt{1+|\mu|^2} |\rho|^2 - |\mu|^2 - |\rho|^2 \mathbf{E}[wz^*] \end{aligned} \right\} \quad (54)$$

$$= \mu\rho. \quad (55)$$

$$\langle \alpha_{12}, \alpha_{11} \rangle = \frac{\mathbf{E}[\alpha_{12}\alpha_{11}^*]}{\sigma_{\alpha_{12}}\sigma_{\alpha_{11}}} \quad (56)$$

$$= \frac{\mathbf{E}\left[\left(\sigma_{\alpha_{12}}\rho^*w + \sigma_{\alpha_{12}}\sqrt{1-|\rho|^2}x\right)\left(\sigma_{\alpha_{11}}w\right)^*\right]}{\sigma_{\alpha_{12}}\sigma_{\alpha_{11}}} \quad (57)$$

$$= \frac{\sigma_{\alpha_{12}}\sigma_{\alpha_{11}}\rho^*\mathbf{E}[ww^*] + \sigma_{\alpha_{12}}\sigma_{\alpha_{11}}\sqrt{1-|\rho|^2}\mathbf{E}[xw^*]}{\sigma_{\alpha_{12}}\sigma_{\alpha_{11}}} \quad (58)$$

$$= \rho^* \quad (59)$$

$$\langle \alpha_{12}, \alpha_{12} \rangle = \frac{\mathbf{E}[\alpha_{12}\alpha_{12}^*]}{\sigma_{\alpha_{12}}^2} \quad (60)$$

$$= \frac{\mathbf{E}\left[\left(\sigma_{\alpha_{12}}\rho^*w + \sigma_{\alpha_{12}}\sqrt{1-|\rho|^2}x\right)\left(\sigma_{\alpha_{12}}\rho^*w + \sigma_{\alpha_{12}}\sqrt{1-|\rho|^2}x\right)^*\right]}{\sigma_{\alpha_{12}}^2} \quad (61)$$

$$= \frac{1}{\sigma_{\alpha_{12}}^2} \left\{ \begin{array}{l} \sigma_{\alpha_{12}}^2 |\rho|^2 \mathbf{E}[ww^*] + \sigma_{\alpha_{12}}^2 \rho^* \sqrt{1-|\rho|^2} \mathbf{E}[wx^*] \\ + \sigma_{\alpha_{12}}^2 \rho \sqrt{1-|\rho|^2} \mathbf{E}[xw^*] + \sigma_{\alpha_{12}}^2 [1-|\rho|^2] \mathbf{E}[xx^*] \end{array} \right\} \quad (62)$$

$$= |\rho|^2 + [1-|\rho|^2] \quad (63)$$

$$= 1 \quad (64)$$

$$\langle \alpha_{12}, \alpha_{21} \rangle = \frac{\mathbf{E}[\alpha_{12}\alpha_{21}^*]}{\sigma_{\alpha_{12}}\sigma_{\alpha_{21}}} \quad (65)$$

$$= \frac{\mathbf{E}\left[\left(\sigma_{\alpha_{12}}\rho^*w + \sigma_{\alpha_{12}}\sqrt{1-|\rho|^2}x\right)\left(\sigma_{\alpha_{21}}\mu^*w + \sigma_{\alpha_{21}}\sqrt{1-|\mu|^2}y\right)^*\right]}{\sigma_{\alpha_{12}}\sigma_{\alpha_{21}}} \quad (66)$$

$$= \frac{1}{\sigma_{\alpha_{12}}\sigma_{\alpha_{21}}} \left\{ \begin{array}{l} \sigma_{\alpha_{12}}\sigma_{\alpha_{21}}\mu\rho^*\mathbf{E}[ww^*] + \sigma_{\alpha_{12}}\sigma_{\alpha_{21}}\rho^*\sqrt{1-|\mu|^2}\mathbf{E}[wy^*] \\ + \sigma_{\alpha_{12}}\sigma_{\alpha_{21}}\mu\sqrt{1-|\rho|^2}\mathbf{E}[xw^*] + \sigma_{\alpha_{12}}\sigma_{\alpha_{21}}\sqrt{1-|\mu|^2}\sqrt{1-|\rho|^2}\mathbf{E}[xy^*] \end{array} \right\} \quad (67)$$

$$= \mu\rho^* \quad (68)$$

$$\langle \alpha_{12}, \alpha_{22} \rangle = \frac{\mathbf{E}[\alpha_{12}\alpha_{22}^*]}{\sigma_{\alpha_{12}}\sigma_{\alpha_{22}}} \quad (69)$$

$$= \frac{\mathbf{E}\left[\left(\sigma_{\alpha_{12}}\rho^*w + \sigma_{\alpha_{12}}\sqrt{1-|\rho|^2}x\right)\left(\sigma_{\alpha_{22}}\mu^*\rho^*w + \sigma_{\alpha_{22}}\mu^*\sqrt{1-|\rho|^2}x + \sigma_{\alpha_{22}}\rho^*\sqrt{1-|\mu|^2}y\right)^*\right]}{\sigma_{\alpha_{12}}\sigma_{\alpha_{22}}} \quad (70)$$

$$= \frac{1}{\sigma_{\alpha_{12}}\sigma_{\alpha_{22}}} \left\{ \begin{array}{l} \sigma_{\alpha_{12}}\sigma_{\alpha_{22}}\mu|\rho|^2\mathbf{E}[ww^*] + \sigma_{\alpha_{12}}\sigma_{\alpha_{22}}\mu\rho^*\sqrt{1-|\rho|^2}\mathbf{E}[wx^*] \\ + \sigma_{\alpha_{12}}\sigma_{\alpha_{22}}\sqrt{1-|\mu|^2}|\rho|^2\mathbf{E}[wy^*] \\ + \sigma_{\alpha_{12}}\sigma_{\alpha_{22}}\rho^*\sqrt{1+|\mu|^2}|\rho|^2 - |\mu|^2 - |\rho|^2\mathbf{E}[wz^*] \\ + \sigma_{\alpha_{12}}\sigma_{\alpha_{22}}\mu\rho\sqrt{1-|\rho|^2}\mathbf{E}[xw^*] + \sigma_{\alpha_{12}}\sigma_{\alpha_{22}}\mu[1-|\rho|^2]\mathbf{E}[xx^*] \\ + \sigma_{\alpha_{12}}\sigma_{\alpha_{22}}\rho\sqrt{1-|\mu|^2}\sqrt{1-|\rho|^2}\mathbf{E}[xy^*] \\ + \sigma_{\alpha_{12}}\sigma_{\alpha_{22}}\sqrt{1-|\rho|^2}\sqrt{1+|\mu|^2}|\rho|^2 - |\mu|^2 - |\rho|^2\mathbf{E}[xz^*] \end{array} \right\} \quad (71)$$

$$= \mu|\rho|^2 + \mu[1-|\rho|^2] \quad (72)$$

$$= \mu. \quad (73)$$

$$\langle \alpha_{21}, \alpha_{11} \rangle = \frac{\mathbf{E}[\alpha_{21} \alpha_{11}^*]}{\sigma_{\alpha_{21}} \sigma_{\alpha_{11}}} \quad (74)$$

$$= \frac{\mathbf{E} \left[\left(\sigma_{\alpha_{21}} \mu^* w + \sigma_{\alpha_{21}} \sqrt{1 - |\mu|^2} y \right) (\sigma_{\alpha_{11}} w)^* \right]}{\sigma_{\alpha_{21}} \sigma_{\alpha_{11}}} \quad (75)$$

$$= \frac{\sigma_{\alpha_{21}} \sigma_{\alpha_{11}} \mu^* \mathbf{E}[ww^*] + \sigma_{\alpha_{21}} \sigma_{\alpha_{11}} \sqrt{1 - |\mu|^2} \mathbf{E}[yw^*]}{\sigma_{\alpha_{21}} \sigma_{\alpha_{11}}} \quad (76)$$

$$= \mu^* \quad (77)$$

$$\langle \alpha_{21}, \alpha_{12} \rangle = \frac{\mathbf{E}[\alpha_{21} \alpha_{12}^*]}{\sigma_{\alpha_{21}} \sigma_{\alpha_{12}}} \quad (78)$$

$$= \frac{\mathbf{E} \left[\left(\sigma_{\alpha_{21}} \mu^* w + \sigma_{\alpha_{21}} \sqrt{1 - |\mu|^2} y \right) \left(\sigma_{\alpha_{12}} \rho^* w + \sigma_{\alpha_{12}} \sqrt{1 - |\rho|^2} x \right)^* \right]}{\sigma_{\alpha_{21}} \sigma_{\alpha_{12}}} \quad (79)$$

$$= \frac{1}{\sigma_{\alpha_{21}} \sigma_{\alpha_{12}}} \left\{ \begin{aligned} & \sigma_{\alpha_{21}} \sigma_{\alpha_{12}} \mu^* \rho \mathbf{E}[ww^*] + \sigma_{\alpha_{21}} \sigma_{\alpha_{12}} \mu^* \sqrt{1 - |\rho|^2} \mathbf{E}[wx^*] \\ & + \sigma_{\alpha_{21}} \sigma_{\alpha_{12}} \rho \sqrt{1 - |\mu|^2} \mathbf{E}[yw^*] + \sigma_{\alpha_{21}} \sigma_{\alpha_{12}} \sqrt{1 - |\rho|^2} \sqrt{1 - |\mu|^2} \mathbf{E}[yx^*] \end{aligned} \right\} \quad (80)$$

$$= \mu^* \rho \quad (81)$$

$$\langle \alpha_{21}, \alpha_{21} \rangle = \frac{\mathbf{E}[\alpha_{21} \alpha_{21}^*]}{\sigma_{\alpha_{21}}^2} \quad (82)$$

$$= \frac{\mathbf{E} \left[\left(\sigma_{\alpha_{21}} \mu^* w + \sigma_{\alpha_{21}} \sqrt{1 - |\mu|^2} y \right) \left(\sigma_{\alpha_{21}} \mu^* w + \sigma_{\alpha_{21}} \sqrt{1 - |\mu|^2} y \right)^* \right]}{\sigma_{\alpha_{21}}^2} \quad (83)$$

$$= \frac{1}{\sigma_{\alpha_{21}}^2} \left\{ \begin{aligned} & \sigma_{\alpha_{21}}^2 |\mu|^2 \mathbf{E}[ww^*] + \sigma_{\alpha_{21}}^2 \mu^* \sqrt{1 - |\mu|^2} \mathbf{E}[wy^*] \\ & + \sigma_{\alpha_{21}}^2 \mu \sqrt{1 - |\mu|^2} \mathbf{E}[yw^*] + \sigma_{\alpha_{21}}^2 [1 - |\mu|^2] \mathbf{E}[yy^*] \end{aligned} \right\} \quad (84)$$

$$= |\mu|^2 + [1 - |\mu|^2] \quad (85)$$

$$= 1 \quad (86)$$

$$\langle \alpha_{21}, \alpha_{22} \rangle = \frac{\mathbf{E}[\alpha_{21} \alpha_{22}^*]}{\sigma_{\alpha_{21}} \sigma_{\alpha_{22}}} \quad (87)$$

$$= \frac{\mathbf{E} \left[\begin{aligned} & \left(\sigma_{\alpha_{21}} \mu^* w + \sigma_{\alpha_{21}} \sqrt{1 - |\mu|^2} y \right) \\ & \left(\sigma_{\alpha_{22}} \mu^* \rho^* w + \sigma_{\alpha_{22}} \mu^* \sqrt{1 - |\rho|^2} x + \sigma_{\alpha_{22}} \rho^* \sqrt{1 - |\mu|^2} y \right)^* \\ & + \sigma_{\alpha_{22}} \sqrt{1 + |\mu|^2 |\rho|^2 - |\mu|^2 - |\rho|^2} z \end{aligned} \right]}{\sigma_{\alpha_{21}} \sigma_{\alpha_{22}}} \quad (88)$$

$$= \frac{1}{\sigma_{\alpha_{21}} \sigma_{\alpha_{22}}} \left\{ \begin{aligned} & \sigma_{\alpha_{21}} \sigma_{\alpha_{22}} \rho |\mu|^2 \mathbf{E}[ww^*] + \sigma_{\alpha_{21}} \sigma_{\alpha_{22}} \sqrt{1 - |\rho|^2} |\mu|^2 \mathbf{E}[wx^*] \\ & + \sigma_{\alpha_{21}} \sigma_{\alpha_{22}} \mu^* \rho \sqrt{1 - |\mu|^2} \mathbf{E}[wy^*] \\ & + \sigma_{\alpha_{21}} \sigma_{\alpha_{22}} \mu^* \sqrt{1 + |\mu|^2 |\rho|^2 - |\mu|^2 - |\rho|^2} \mathbf{E}[wz^*] \\ & + \sigma_{\alpha_{21}} \sigma_{\alpha_{22}} \mu \rho \sqrt{1 - |\mu|^2} \mathbf{E}[yw^*] + \sigma_{\alpha_{21}} \sigma_{\alpha_{22}} \mu \sqrt{1 - |\mu|^2} \sqrt{1 - |\rho|^2} \mathbf{E}[yx^*] \\ & + \sigma_{\alpha_{21}} \sigma_{\alpha_{22}} \rho [1 - |\mu|^2] \mathbf{E}[yy^*] \\ & + \sigma_{\alpha_{21}} \sigma_{\alpha_{22}} \sqrt{1 - |\mu|^2} \sqrt{1 + |\mu|^2 |\rho|^2 - |\mu|^2 - |\rho|^2} \mathbf{E}[yz^*] \end{aligned} \right\} \quad (89)$$

$$= \rho |\mu|^2 + \rho [1 - |\mu|^2] \quad (90)$$

$$= \rho. \quad (91)$$

$$\langle \alpha_{22}, \alpha_{11} \rangle = \frac{\mathbf{E}[\alpha_{22}\alpha_{11}^*]}{\sigma_{\alpha_{22}}\sigma_{\alpha_{11}}} \quad (92)$$

$$= \frac{1}{\sigma_{\alpha_{22}}\sigma_{\alpha_{11}}} \mathbf{E} \left[\left(\begin{array}{l} \sigma_{\alpha_{22}}\mu^*\rho^*w + \sigma_{\alpha_{22}}\mu^*\sqrt{1-|\rho|^2}x \\ + \sigma_{\alpha_{22}}\rho^*\sqrt{1-|\mu|^2}y + \sigma_{\alpha_{22}}\sqrt{1+|\mu|^2|\rho|^2-|\mu|^2-|\rho|^2}z \end{array} \right) \sigma_{\alpha_{11}}w^* \right] \quad (93)$$

$$= \frac{1}{\sigma_{\alpha_{22}}\sigma_{\alpha_{11}}} \left\{ \begin{array}{l} \sigma_{\alpha_{22}}\sigma_{\alpha_{11}}\mu^*\rho^*\mathbf{E}[ww^*] + \sigma_{\alpha_{22}}\sigma_{\alpha_{11}}\mu^*\sqrt{1-|\rho|^2}\mathbf{E}[xw^*] \\ + \sigma_{\alpha_{22}}\sigma_{\alpha_{11}}\rho^*\sqrt{1-|\mu|^2}\mathbf{E}[yw^*] \\ + \sigma_{\alpha_{22}}\sigma_{\alpha_{11}}\sqrt{1+|\mu|^2|\rho|^2-|\mu|^2-|\rho|^2}\mathbf{E}[zw^*] \end{array} \right\} \quad (94)$$

$$= \mu^*\rho^* \quad (95)$$

$$\langle \alpha_{22}, \alpha_{12} \rangle = \frac{\mathbf{E}[\alpha_{22}\alpha_{12}^*]}{\sigma_{\alpha_{22}}\sigma_{\alpha_{12}}} \quad (96)$$

$$= \frac{\mathbf{E} \left[\left(\begin{array}{l} \sigma_{\alpha_{22}}\mu^*\rho^*w + \sigma_{\alpha_{22}}\mu^*\sqrt{1-|\rho|^2}x + \sigma_{\alpha_{22}}\rho^*\sqrt{1-|\mu|^2}y \\ + \sigma_{\alpha_{22}}\sqrt{1+|\mu|^2|\rho|^2-|\mu|^2-|\rho|^2}z \end{array} \right) \left(\begin{array}{l} \sigma_{\alpha_{12}}\rho^*w + \sigma_{\alpha_{12}}\sqrt{1-|\rho|^2}x \end{array} \right)^* \right]}{\sigma_{\alpha_{22}}\sigma_{\alpha_{12}}} \quad (97)$$

$$= \frac{1}{\sigma_{\alpha_{22}}\sigma_{\alpha_{12}}} \left\{ \begin{array}{l} \sigma_{\alpha_{22}}\sigma_{\alpha_{12}}\mu^*|\rho|^2\mathbf{E}[ww^*] + \sigma_{\alpha_{22}}\sigma_{\alpha_{12}}\mu^*\rho\sqrt{1-|\rho|^2}\mathbf{E}[xw^*] \\ + \sigma_{\alpha_{22}}\sigma_{\alpha_{12}}\sqrt{1-|\mu|^2}|\rho|^2\mathbf{E}[yw^*] \\ + \sigma_{\alpha_{22}}\sigma_{\alpha_{12}}\rho\sqrt{1+|\mu|^2|\rho|^2-|\mu|^2-|\rho|^2}\mathbf{E}[zw^*] \\ + \sigma_{\alpha_{22}}\sigma_{\alpha_{12}}\mu^*\rho^*\sqrt{1-|\rho|^2}\mathbf{E}[wz^*] + \sigma_{\alpha_{22}}\sigma_{\alpha_{12}}\mu^*[1-|\rho|^2]\mathbf{E}[xx^*] \\ + \sigma_{\alpha_{22}}\sigma_{\alpha_{12}}\rho^*\sqrt{1-|\mu|^2}\sqrt{1-|\rho|^2}\mathbf{E}[yx^*] \\ + \sigma_{\alpha_{22}}\sigma_{\alpha_{12}}\sqrt{1-|\rho|^2}\sqrt{1+|\mu|^2|\rho|^2-|\mu|^2-|\rho|^2}\mathbf{E}[zx^*] \end{array} \right\} \quad (98)$$

$$= \mu^*|\rho|^2 + \mu^*[1-|\rho|^2] \quad (99)$$

$$= \mu^* \quad (100)$$

$$\langle \alpha_{22}, \alpha_{21} \rangle = \frac{\mathbf{E}[\alpha_{22}\alpha_{21}^*]}{\sigma_{\alpha_{22}}\sigma_{\alpha_{21}}} \quad (101)$$

$$= \frac{\mathbf{E} \left[\left(\begin{array}{l} \sigma_{\alpha_{22}}\mu^*\rho^*w + \sigma_{\alpha_{22}}\mu^*\sqrt{1-|\rho|^2}x + \sigma_{\alpha_{22}}\rho^*\sqrt{1-|\mu|^2}y \\ + \sigma_{\alpha_{22}}\sqrt{1+|\mu|^2|\rho|^2-|\mu|^2-|\rho|^2}z \end{array} \right) \left(\begin{array}{l} \sigma_{\alpha_{21}}\mu^*w + \sigma_{\alpha_{21}}\sqrt{1-|\mu|^2}y \end{array} \right)^* \right]}{\sigma_{\alpha_{22}}\sigma_{\alpha_{21}}} \quad (102)$$

$$= \frac{1}{\sigma_{\alpha_{22}}\sigma_{\alpha_{21}}} \left\{ \begin{array}{l} \sigma_{\alpha_{22}}\sigma_{\alpha_{21}}\rho^*|\mu|^2\mathbf{E}[ww^*] + \sigma_{\alpha_{22}}\sigma_{\alpha_{21}}\sqrt{1-|\rho|^2}|\mu|^2\mathbf{E}[xw^*] \\ + \sigma_{\alpha_{22}}\sigma_{\alpha_{21}}\mu\rho^*\sqrt{1-|\mu|^2}\mathbf{E}[yw^*] \\ + \sigma_{\alpha_{22}}\sigma_{\alpha_{21}}\mu\sqrt{1+|\mu|^2|\rho|^2-|\mu|^2-|\rho|^2}\mathbf{E}[zw^*] \\ + \sigma_{\alpha_{22}}\sigma_{\alpha_{21}}\mu^*\rho^*\sqrt{1-|\mu|^2}\mathbf{E}[wy^*] \\ + \sigma_{\alpha_{22}}\sigma_{\alpha_{21}}\mu^*\sqrt{1-|\mu|^2}\sqrt{1-|\rho|^2}\mathbf{E}[xy^*] \\ + \sigma_{\alpha_{22}}\sigma_{\alpha_{21}}\rho^*[1-|\mu|^2]\mathbf{E}[yy^*] \\ + \sigma_{\alpha_{22}}\sigma_{\alpha_{21}}\sqrt{1-|\mu|^2}\sqrt{1+|\mu|^2|\rho|^2-|\mu|^2-|\rho|^2}\mathbf{E}[zy^*] \end{array} \right\} \quad (103)$$

$$= \rho^*|\mu|^2 + \rho^*[1-|\mu|^2] \quad (104)$$

$$= \rho^* \quad (105)$$

$$\langle \alpha_{22}, \alpha_{22} \rangle = \frac{\mathbf{E}[\alpha_{22}\alpha_{22}^*]}{\sigma_{\alpha_{22}}^2} \quad (106)$$

$$= \frac{\mathbf{E} \left[\begin{pmatrix} \sigma_{\alpha_{22}}\mu^*\rho^*w + \sigma_{\alpha_{22}}\mu^*\sqrt{1-|\rho|^2}x + \sigma_{\alpha_{22}}\rho^*\sqrt{1-|\mu|^2}y \\ +\sigma_{\alpha_{22}}\sqrt{1+|\mu|^2|\rho|^2-|\mu|^2-|\rho|^2}z \\ \sigma_{\alpha_{22}}\mu^*\rho^*w + \sigma_{\alpha_{22}}\mu^*\sqrt{1-|\rho|^2}x + \sigma_{\alpha_{22}}\rho^*\sqrt{1-|\mu|^2}y \\ +\sigma_{\alpha_{22}}\sqrt{1+|\mu|^2|\rho|^2-|\mu|^2-|\rho|^2}z \end{pmatrix}^* \right]}{\sigma_{\alpha_{22}}^2} \quad (107)$$

$$= \frac{1}{\sigma_{\alpha_{22}}^2} \left\{ \begin{array}{l} \sigma_{\alpha_{22}}^2 |\mu|^2 |\rho|^2 \mathbf{E}[ww^*] + \sigma_{\alpha_{22}}^2 |\mu|^2 \rho \sqrt{1-|\rho|^2} \mathbf{E}[xw^*] \\ + \sigma_{\alpha_{22}}^2 \mu |\rho|^2 \sqrt{1-|\mu|^2} \mathbf{E}[yw^*] + \sigma_{\alpha_{22}}^2 \mu \rho \sqrt{1+|\mu|^2|\rho|^2-|\mu|^2-|\rho|^2} \mathbf{E}[zw^*] \\ + \sigma_{\alpha_{22}}^2 |\mu|^2 \rho \sqrt{1-|\rho|^2} \mathbf{E}[wx^*] + \sigma_{\alpha_{22}}^2 |\mu|^2 [1-|\rho|^2] \mathbf{E}[xx^*] \\ + \sigma_{\alpha_{22}}^2 \mu \rho^* \sqrt{1-|\mu|^2} \sqrt{1-|\rho|^2} \mathbf{E}[yx^*] \\ + \sigma_{\alpha_{22}}^2 \mu \sqrt{1-|\rho|^2} \sqrt{1+|\mu|^2|\rho|^2-|\mu|^2-|\rho|^2} \mathbf{E}[zx^*] \\ + \sigma_{\alpha_{22}}^2 \mu^* |\rho|^2 \sqrt{1-|\mu|^2} \mathbf{E}[wy^*] + \sigma_{\alpha_{22}} \sigma_{\alpha_{22}} \mu^* \rho \sqrt{1-|\mu|^2} \sqrt{1-|\rho|^2} \mathbf{E}[xy^*] \\ + \sigma_{\alpha_{22}}^2 |\rho|^2 [1-|\mu|^2] \mathbf{E}[yy^*] \\ + \sigma_{\alpha_{22}}^2 \rho \sqrt{1-|\mu|^2} \sqrt{1+|\mu|^2|\rho|^2-|\mu|^2-|\rho|^2} \mathbf{E}[zy^*] \\ \sigma_{\alpha_{22}}^2 \mu^* \rho^* \sqrt{1+|\mu|^2|\rho|^2-|\mu|^2-|\rho|^2} \mathbf{E}[wz^*] \\ + \sigma_{\alpha_{22}}^2 \mu^* \sqrt{1-|\rho|^2} \sqrt{1+|\mu|^2|\rho|^2-|\mu|^2-|\rho|^2} \mathbf{E}[xz^*] \\ + \sigma_{\alpha_{22}}^2 \rho^* \sqrt{1-|\mu|^2} \sqrt{1+|\mu|^2|\rho|^2-|\mu|^2-|\rho|^2} \mathbf{E}[yz^*] \\ + \sigma_{\alpha_{22}}^2 [1+|\mu|^2|\rho|^2-|\mu|^2-|\rho|^2] \mathbf{E}[zz^*] \end{array} \right\} \quad (108)$$

$$= |\mu|^2 |\rho|^2 + |\mu|^2 [1-|\rho|^2] + |\rho|^2 [1-|\mu|^2] + [1+|\mu|^2|\rho|^2-|\mu|^2-|\rho|^2] \quad (109)$$

$$= 1. \quad (110)$$

ACKNOWLEDGMENT

The authors appreciate the useful comments from the anonymous reviewers.

REFERENCES

- [1] G. J. Foschini, "Layered space-time architecture for wireless communication in fading environment when using multi-element antennas," *Bell Labs Tech. J.*, pp. 41–59, Autumn 1996.
- [2] G. G. Raleigh and J. M. Cioffi, "Spatio-temporal coding for wireless communication," *IEEE Trans. Commun.*, vol. 46, pp. 357–366, Mar. 1998.
- [3] I. E. Telatar. (1995) Capacity of Multi-Antenna Gaussian Channels. AT&T Bell Labs. [Online]. Available: <http://mars.bell-labs.com/cm/ms/what/mars/papers/proof>
- [4] D. Gesbert, H. Boleskei, D. Gore, and A. Paulraj, "MIMO wireless channels: Capacity and performance prediction," in *Proc. GLOBECOM'00*, vol. 2, San Francisco, USA, Nov. 2000, pp. 1083–1088.
- [5] D. S. Shiu, *Wireless Communication Using Dual Antenna Array*. Norwell, MA: Kluwer, 2000.
- [6] W. C. Jakes, *Microwave Mobile Communications*. New York: Wiley, 1974.
- [7] K. I. Pedersen, J. B. Andersen, J. P. Kermoal, and P. E. Mogensen, "A stochastic multiple-input multiple-output radio channel model for evaluation of space-time coding algorithms," in *Proc. Vehicular Technology Conf.*, Boston, MA, Sept. 2000, pp. 893–897.
- [8] R. B. Ertel, P. Cardieri, K. W. Sowerby, T. S. Rappaport, and J. H. Reed, "Overview of spatial channel models for antenna array communication systems," *IEEE Pers. Commun.*, pp. 10–21, Feb. 1998.
- [9] J. Liberti and T. Rappaport, "A geometrically based model for line-of-sight multipath radio channels," in *Proc. Vehicular Technology Conf.*, Atlanta, Georgia, Apr. 1996, pp. 844–848.
- [10] O. Nørklit and J. B. Andersen, "Diffuse channel model and experimental results for antenna arrays in mobile environments," *IEEE Trans. Antennas Propagat.*, vol. 46, pp. 834–840, June 1998.
- [11] P. Eggers, "Angular dispersive mobile radio environments sensed by highly directive base station antennas," in *Proc. PIMRC'95*, Toronto, Canada, Sept. 1995, pp. 522–526.
- [12] K. I. Pedersen and P. E. Mogensen, "Simulation of dual-polarized propagation environments for adaptive antennas," in *Proc. Vehicular Technology Conf.*, Amsterdam, Netherlands, Sept. 1999, pp. 62–66.
- [13] B. H. Fleury, "First- and second-order characterization of direction dispersion and space selectivity in the radio channel," *IEEE Trans. Inform. Theory*, vol. 46, pp. 2027–2044, Sept. 2000.
- [14] W. C. Y. Lee, "Effects on correlation between two mobile radio base-station antennas," *IEEE Trans. Commun.*, vol. 21, pp. 1214–1224, Nov. 1973.
- [15] F. Adachi, M. Feeny, A. Williamson, and J. Parsons, "Crosscorrelation between the envelopes of 900 MHz signals received at a mobile radio base station site," *Proc. Inst. Elect. Eng.*, pt. F, vol. 133, pp. 506–512, Oct. 1986.
- [16] J. Salz and J. Winters, "Effect of fading correlation on adaptive arrays in digital mobile radio," *IEEE Trans. Veh. Technol.*, vol. 43, pp. 1049–1057, Nov. 1994.
- [17] K. I. Pedersen, P. E. Mogensen, and B. H. Fleury, "Spatial channel characteristics in outdoor environments and their impact on BS antenna system performance," in *Proc. Vehicular Technology Conf.*, Ottawa, Canada, May 1998, pp. 719–724.
- [18] G. Durgin and T. S. Rappaport, "Basic relationship between multipath angular spread and narrowband fading in wireless channels," *Electron. Lett.*, vol. 34, pp. 2431–2432, Dec. 1998.

- [19] —, "Effects of multipath angular spread on the spatial cross-correlation of received voltage envelopes," in *Proc. Vehicular Technology Conf.*, Houston, TX, May 1999, pp. 996–1000.
- [20] K. Yu, M. Bengtsson, B. Ottersten, D. McNamara, P. Karlsson, and M. Beach, "Second order statistics of NLOS indoor MIMO channels based on 5.2 GHz measurements," in *Proc. GLOBECOM'01*, San Antonio, Texas, USA, Nov. 2001, pp. 156–160.
- [21] P. Petrus, J. H. Reed, and T. S. Rappaport, "Effects of directional antennas at the base station on the Doppler spectrum," *IEEE Commun. Lett.*, vol. 1, pp. 40–42, Mar. 1997.
- [22] D. Chizhik, G. J. Foschini, and R. A. Valenzuela, "Capacities of multi-element transmit and receive antennas: Correlations and Keyholes," *Electron. Lett.*, vol. 36, pp. 1099–1100, June 2000.
- [23] J. P. Kermoal, P. E. Mogensen, S. H. Jensen, J. B. Andersen, F. Frederiksen, T. B. Sørensen, and K. I. Pedersen, "Experimental investigation of multipath richness for multi-element transmit and receive antenna arrays," in *Proc. Vehicular Technology Conf.*, Tokyo, Japan, May 2000, pp. 2004–2008.
- [24] J. P. Kermoal, L. Schumacher, P. E. Mogensen, and K. I. Pedersen, "Experimental investigation of correlation properties of MIMO radio channels for indoor picocell scenarios," in *Proc. Vehicular Technology Conf.*, Boston, MA, Sept. 2000, pp. 14–21.
- [25] F. Frederiksen, P. Mogensen, K. I. Pedersen, and P. Leth-Espensen, "A "Software" testbed for performance evaluation of adaptive antennas in FH GSM and wideband-CDMA," in *Conf. Proc. 3rd ACTS Mobile Communication Summit*, vol. 2, Rhodes, Greece, June 1998, pp. 430–435.
- [26] J. B. Andersen, "Array gain and capacity for known random channels with multiple element arrays at both ends," *IEEE J. Select. Areas Commun.*, vol. 18, pp. 2172–2178, Nov. 2000.
- [27] S. Haykin, *Adaptive Filter Theory*. Upper Saddle River, NJ: Prentice-Hall, 1991.
- [28] G. H. Golub and C. F. Van Loan, *Matrix Computations*, 3rd ed. Baltimore, MD: The Johns Hopkins Univ. Press, 1996.



Laurent Schumacher (M'96) was born in Mons, Belgium, in 1971. He received the M.Sc. E.E. degree from the Faculté Polytechnique de Mons, Belgium, in 1993 and the Ph.D. degree from the Université catholique de Louvain, Belgium, in 1999.

He then joined the Center for PersonKommunikation (CPK), Aalborg University, Aalborg, Denmark, where he has been appointed as Associate Research Professor. His current research interests are the design of MIMO radio channel models and the investigation of advanced algorithms and techniques for the delivery of high bit-rate services in cellular systems (UMTS and beyond).



Klaus Ingemann Pedersen (S'97–M'00) received the M.Sc. E.E. and Ph.D. degrees, in 1996 and 2000, respectively, from Aalborg University, Aalborg, Denmark.

He is currently with Nokia Networks, Aalborg, Denmark. His current research interests include radio resource managements for WCDMA systems, adaptive antenna array systems, and radio propagation.



Preben Elgaard Mogensen (S'88–M'00) received the M.Sc. E.E. and Ph.D. degrees, in 1988 and 1996, respectively, from Aalborg University, Aalborg, Denmark.

Since 1988, he has been with Aalborg University. He is currently holding a part time position as Research Professor and heading the cellular Systems Research Group (CSYS) at the Center for Personkommunikation (CPK). Since 1995, he has been working part time with Nokia Networks, Aalborg, Denmark, and is now Manager of the 3G Radio

Systems Research team at NET/Aalborg.



Jean Philippe Kermoal was born in Paris, France, in 1972. He received the M.Phil. degree from the University of Glamorgan, U.K., in 1998. He is currently working towards the Ph.D. degree in multi-element transmit and receive antenna arrays for wireless communication systems at Aalborg University, Aalborg, Denmark.

His research interests include MIMO radio channel characterization, adaptive antenna array, and indoor and outdoor mobile communication propagation at microwave and millimeter-wave band.



Frank Frederiksen received the M.Sc.E.E. degree in telecommunications from Aalborg University, Aalborg, Denmark, in 1994.

From 1994 to 2000, he has been working at the Center for Personkommunikation, Aalborg University as a Research Engineer developing measurement systems for DECT/GSM/W-CDMA. Since 2000, he has been working for Nokia Networks, Aalborg, Denmark, on evaluation of high speed data services for W-CDMA.